10-10-2020

Modeling of the Electrical Characteristics of an Organic Field Effect Transistor in Presence of the Bending Effects

Yi Yang
Purdue University, yang1087@purdue.edu

Robert Nawrocki
Purdue University, robertnawrocki@purdue.edu

Richard Voyles
Purdue University, rvoyles@purdue.edu

Haiyan H. Zhang
Purdue University, hhzhang@purdue.edu

Recommended Citation

Yang, Yi, Robert A. Nawrocki, Richard M. Voyles and Haiyan Zhang. "Modeling of the electrical characteristics of an organic field effect transistor in presence of the bending effects." Organic Electronics 88 (2021): 106000.

Modeling of the Electrical Characteristics of an Organic Field Effect Transistor in Presence of the Bending Effects

Yi Yang, Robert A. Nawrocki, Richard M. Voyles, and Haiyan H. Zhang

Abstract—An analytical model incorporating the density of trap states for a bendable organic field effect transistor (OFET) is presented in this paper. The aim of this work is to propose a novel modeling framework to quantitatively characterize the bending effects on the electrical properties of an OFET in the linear and saturation regimes. In this model, the exponentially distributed shallow trap states are introduced into the Poisson equation to describe the carrier transports in the channel. The carrier mobility takes into account the low field mobility enhancement under gradual channel approximation and high field degradation. As a result, the generalized current-voltage transistor equations are derived for the first time to reflect the transconductance relationships of the OFET with trap states. In addition, an electro-mechanical coupling relationship is established per the metaphorical analogy between inorganic and organic semiconductor energy band models to quantify the stress-induced variations of the carrier mobility, and the threshold voltage. It is revealed that the before- and after-bending transconductances, predicted from the derived analytical model, are in good agreement with the experimental data measured from DNTT-based OFET bending tests.

Index Terms—Bending stress, carrier mobility, density of trap states, electro-mechanical coupling relationship, organic thin-film transistor, transconductance.

I. Introduction

ORGANIC thin-film transistors (OFETs) are fast becoming an intensive research topic, over the last few decades, due to its extensive applications in the manufacturing of biocompatible and stretchable sensors or actuators [1]–[9]. The rapid development of OFETs is not aimed at achieving the same-level circuit performance brought by the silicon-based transistors, but at reducing the cost of low-end electronics by its potential to replace silicon with potentially inexpensive organic alternatives [10]. Another benefit of OFETs, compared to inorganic TFTs, is their unprecedented physical flexibility [11]–[13]. The commercial deployment of physically flexible organic electronics requires a fast and accurate gauge of OFET-based circuit performance in the process of electronic design automation (EDA), but investigating the analytical model of the OFET is a continuing concern within the semiconductor industry. A considerable amount of literature has been published on the modeling of OFETs. Initial analysis of OFETs relied on models developed for MOSFETs [14]–[19]. However, they cannot accurately describe complex OFET behavior, for instance determining the threshold voltage V_{th} and mobility μ, as they do not incorporate effects such as trap states nor the intrinsic difference between MOSFETs and OFETs. It was shown in [20]–[22] that the OFET's field-effect mobility extracted from the standard MOSFET equations is significantly overestimated. Former investigators have examined the effects of trap states on the modeling of OFETs. For instance, the finite element based program was developed in software device simulation Silvaco to solve the carrier transport equations with trap effects [23]. In a later work, a Matlab based analytic model with trap states was also developed, and it was shown that both the Matlab and finite element analysis models exhibit a good agreement with reported experimental measurements [24]. Up to date, multiple trap-states OFET models have been proposed, including the variable-range hopping transport model with double-exponential trap states [25], the surface potential based HiSIM-Org model [26], the compact OFET models with variable channel length or variable density of trap states [27], [28], the low-voltage Pentacene based UOFET model [29], and the experimental verification of density of trap states in OFETs [30], [31]. Granting the improved accuracy in the characterization of OFET's electrical properties provided by these OFET models by considering the effects of trap states, a generalization of the OFET's transconductance characteristics and effective mobility model is still largely missing. Furthermore, there are few studies to date that have investigated the association between mechanical deformations and the stress-induced variations of OFET's electrical properties. Although some research has been carried out on the strain-induced electrical characterization of MOSFETs by resorting to quantum theory [32]–[38], the precise physical formulation of electro-mechanical coupling relationship within the organic

Y. Yang, R. A. Nawrocki, R. M. Voyles, and H. H. Zhang are with the School of Engineering Technology, Purdue University, West Lafayette, IN 47907 USA (emails: yang1087, robertnawrocki, rvoyles, hhzhang@purdue.edu).
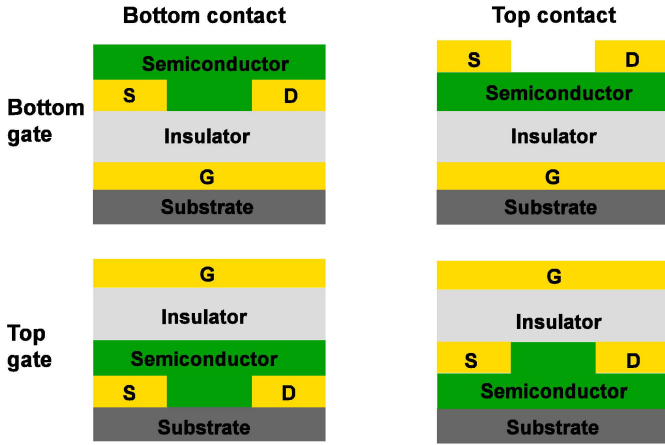
Fig. 1. The structural schematic of a BGTC OFET.

semiconductors (OSCs) still remains a challenge. The development of cheap, light, thin and flexible electronics necessitates the precise modeling of OFETs under mechanical deformations. This work was motivated by the need to develop a generalized transconductance characteristics and its associated mobility model in presence of the bending effects on the OFET.

In this work, we propose a novel compact model for a DNTT-based (a p-type OSC) OFET. In this model, we show that the OFET's effective mobility is enhanced in the low field region and degraded in the high field region due to drift velocity saturation and effects of trap states. The current-voltage characteristic equations are generalized for the first time to account for the existence of tail donor-type trap states. The bending-induced shifts on the effective mobility and the threshold voltage follow a group of semi-empirical equations by analogously applying strained theories developed for MOSFETs. The model is verified by showing that it is in a good agreement with a measured DNTT-based OFET under bending. This work is likely the first to explore the physical modeling of a bendable OFET. The modeling approach developed in our work facilitates the electrical characterization of OFETs and foster the industrial procedures of EDA for flexible electronics.

II. STRUCTURES AND COMPACT MODEL OF OFET

The OFETs are typically made up of three types of materials: the electrode conductors, dielectric insulators, and the OSCs. As shown in Fig. 1, OFETs have four different layouts [39]. Because compared with the other layouts the bottom-gate, top-contact (BGTC) OFET demonstrated improved performance, specifically its carrier mobility and the I_{on}/I_{off} ratio, in this study, the BGTC OFET is presented for analysis [40]. However, it should be mentioned that the modeling approach proposed in this work is applicable to the other three types of OFETs as well.

In the BGTC OFET, the two neighboring electrodes (source and drain islands) are patterned on top of the soft OSC dinaphtho[2,3b:2',3'-f]thieno[3,2-b]thiophene (DNTT), and the dielectric layer (Parylene) is positioned below and isolating the semiconductor from the bottom gate. The OSC materials are
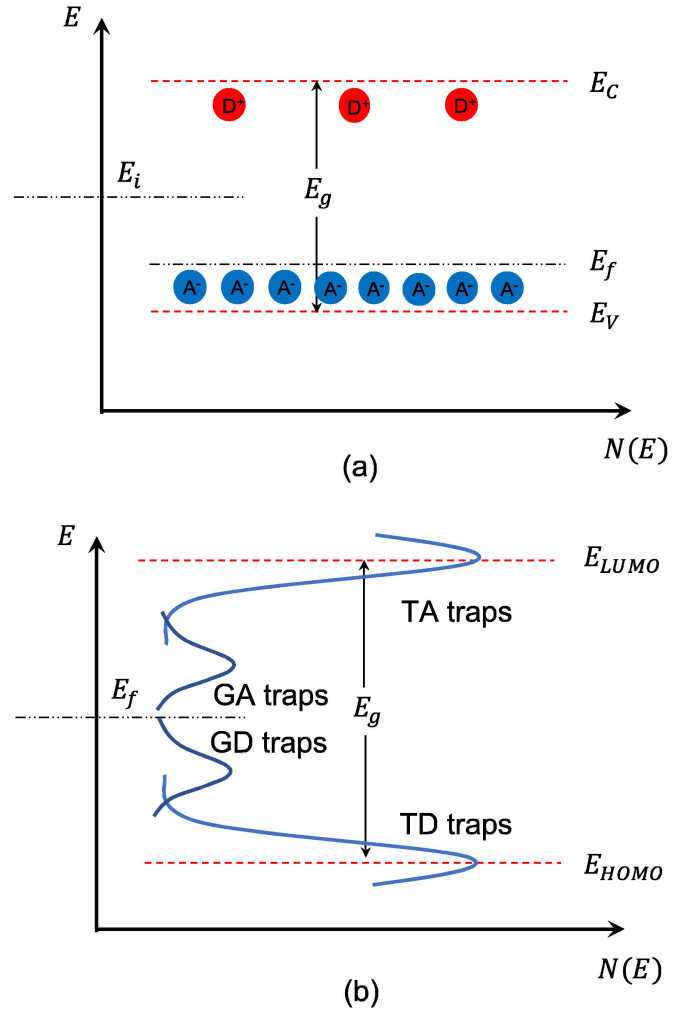

Fig. 2. (a) Simplified energy band diagram for a p-type inorganic semiconductor with ionized donor sites (red) and ionized acceptor sites (blue). (b) Simplified energy band diagram for a p-type organic semiconductor with continuous distributions of deep and shallow trap states, $N(E)$ is the density of states at energy level E.

conducting polymers or irregular crystalline (polycrystalline or amorphous) with grained boundaries. In contrast to traditional inorganic semiconductors (ISC, e.g., Si, Ge, As, etc.), OSCs (organic materials include small and large molecules, such as polymers) are mainly macromolecules with carbon as core elements and possess localized trap Energy levels due to strong σ and π bonds formed by carbon atoms. In ISCs, it is a convention to name the lowest energy level for mobile holes or electrons as valence band (E_v) and conduction band (E_c), respectively. Per the metaphorical analogy, the OSCs have two important energy levels HOMO (Highest Occupied Molecular Orbit) and LUMO (Lowest Unoccupied Molecular Orbit), which forms the bandgap $E_g = E_{LUMO} - E_{HOMO}$.

A detailed comparison for the energy diagrams of organic and inorganic semiconductors is shown in Fig. 2. As displayed in Fig. 2, the OSCs contain a substantial number of trap energy levels (i.e., trap states) in the bandgap, while the ISCs do not. According to the charge properties, the trap states are divided into two classes: the donor-type trap states that are distributed

near LUMO, and the acceptor-type trap states that are located around HOMO. Due to their specific positions in the energy gap, the donor-type trap levels can capture holes from LUMO, and the acceptor-type trap levels can seize electrons from HOMO. The massive number of trap levels in the OSCs reduces the number of majority carriers in the accumulation layer of the semiconductor channel and thereby limits the current conduction capability in OFET. In the modeling of OFET, both of the density of states (i.e., holes and electrons) and the density of trap states (i.e., donor-type and acceptor-type trap states) need considering.

A. Carrier Density and Surface Potential Modeling

For a semiconductor in equilibrium conditions, the carrier concentrations n and p are temperature dependent and given in (1) and (2),

$$n(T) = N_l(T) \exp\left(-\frac{E_{LUMO} - E_f}{kT}\right) \tag{1}$$

$$p(T) = N_h(T) \exp\left(-\frac{E_f - E_{HOMO}}{kT}\right) \tag{2}$$

where N_l and N_h are effective density of states (DoS) in LUMO and HOMO band, respectively, and are constants depending on electron effective mass, pole effective mass and temperature. E_f is the Fermi level, k is the Boltzmann constant and T is the temperature in Kelvin. In the derivation of charge carriers' concentrations, it is assumed that the semiconductor is nondegenerate and Boltzmann statistics can be applied to specify the probability that an available state at an energy level E will be occupied by a charge carrier. This nondegeneracy assumption is valid for an OSC since it is usually undoped, making its Fermi level more than $3kT$ away from both the HOMO and LUMO levels. The product of electron and pole concentrations establishes an important formula that describes the carrier concentration n_i in the intrinsic semiconductor, as shown in (3).

$$n_i^2 = n(T)p(T) = N_l(T)N_h(T) \exp\left(-\frac{E_g}{kT}\right) \tag{3}$$

As shown in Fig. 2, regardless of the acceptor- or donor-type, the trap states in deep levels are approximated by Gaussian distribution and the shallow trap states by exponential distribution. The density of states for tail/shallow-level acceptor-type (TA), tail-level donor-type (TD), deep-level acceptor-type (GA) and deep-level donor-type (GD) traps are respectively given in (4)-(7),

$$g_{TA}(E) = N_{TA} \exp\left(\frac{E - E_{LUMO}}{w_{TA}}\right) \tag{4}$$

$$g_{TD}(E) = N_{TD} \exp\left(\frac{E_{HOMO} - E}{w_{TD}}\right) \tag{5}$$

$$g_{GA}(E) = N_{GA} \exp\left(-\left(\frac{E_{GA} - E}{w_{GA}}\right)^2\right) \tag{6}$$

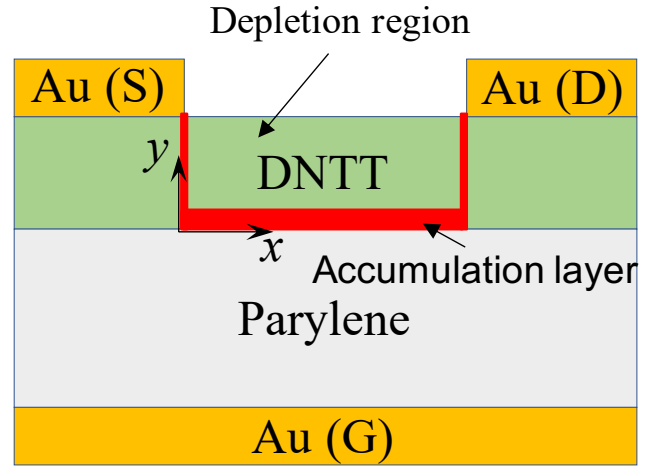$$g_{GD}(E) = N_{GD} \exp\left(-\left(\frac{E_{GD} - E}{w_{GD}}\right)^2\right) \tag{7}$$

Fig. 3. The anatomical structure of a BGTC OFET with coordinate system positioning along the active channel.

where N_{TA}, N_{TD}, N_{GA} and N_{GD} are band edge intercept densities. w_{TA}, w_{TD}, w_{GA}, w_{GD}, E_{GA} and E_{GD} are physical parameters that need tuning in simulation. For p-type OSCs, the donor-type trap states in the shallow level (i.e., TD traps) are more important than other three types of trap states since TD traps are close to the band edges of HOMO and its continuous trapping and detrapping of free holes from HOMO have a great influence on the majority carrier concentrations in the channel. The ionization probability of trap states is derived from Boltzmann statistical mechanics. Since we focus on the modeling of TD traps for the p-type OSCs in our study, we only present the ionization probability function $f_{TD}(E)$ for TD traps, as given in (8).

$$f_{TD}(E) = \frac{1}{1 + \exp\left(\frac{E - E_f}{kT}\right)} \tag{8}$$

In order to obtain the ionized density of trap states, we need to evaluate the integral $\int_{-\infty}^{+\infty} g_{TD}(E)(1 - f_{TD}(E))dE$. Here, we let $w_{TD} = kT_1$, where T_1 is the characteristic temperature for TD trap states. It can be easily verified that the integral is divergent if $T_1 < T$. Then, the integral is evaluated for $T_1 \geq T$, and the ionized density of TD trap sates is given in (9),

$$g_{TD}^+ = N_{TD0}(T) \exp\left(\frac{E_{HOMO} - E_f}{kT_1}\right) \tag{9}$$

and the edge intercept $N_{TD0}(T)$ of ionized TD trap states is given in (10),

$$N_{TD0}(T) = \alpha(T)N_{TD}\frac{k^2 T_1^2}{kT_1 - kT} \tag{10}$$

where $\alpha(T)$ is a dimensionless parameter depending solely on the temperature to compensate the integration errors, and $\alpha(T) = 0.8 \sim 1$.

We consider a BGTC OFET with its anatomical structure shown in Fig. 3. When the bias voltage is applied to the gate electrode, the majority carriers may concentrate in a thin channel (typically only few angstroms for OSCs) near the dielectric-semiconductor interface, and this thin channel is called the accumulation layer (the red part in Fig. 3) of the OFET. The Poisson's equation is then utilized to describe the electric potentials in the semiconductor, as given in (11),

$$\nabla^2 \varphi = -\frac{q}{\varepsilon_s}(p - n + N_D^+ - N_A^-) \tag{11}$$

where φ is the electric potential in the semiconductor, N_D^+ is the concentration of ionized donor-type particles, and N_A^- is the concentration of ionized acceptor-type particles. Since OSC is approximately intrinsic and TD traps are assumed to be the major defect levels in the energy band, we have $n \approx 0, N_A^- \approx 0$, and $N_D^+ \approx g_{TD}^+$. Substituting (2) and (9) into (11) gives the electric field $E(x, y)$ in the OSC, as given in (12),

$$E(x, y) = \sqrt{\frac{2kTN_h}{\varepsilon_s}} \cdot F(\varphi) \tag{12}$$

where the electric potential $\varphi(x, y)$ is evaluated from implicit potential function $F(\varphi)$ given in (13).

$$F(\varphi) = \left[\left(e^{-\frac{q\varphi}{kT}} + \frac{q\varphi}{kT} - 1 \right) + \frac{n_i^2}{N_h^2} \left(e^{\frac{q\varphi}{kT}} - \frac{q\varphi}{kT} - 1 \right) \right. \\ \left. + \frac{N_{TD0}T_1}{N_h T} \left(e^{-\frac{q\varphi}{kT_1}} - 1 \right) \right]^{1/2} \tag{13}$$

If we let $y = 0$, the surface potential $\varphi_s = \varphi(x, 0)$ can be obtained. By considering the continuity of charge flux on the dielectric-semiconductor interface, the gate voltage V_{gs} can be analytically solved and it is given in (14).

$$V_{gs} = \varphi_s + \frac{K_S}{K_O} x_o E_s + V_{fb} \tag{14}$$

where K_S, K_O are the dielectric constants of the OSC and Parylene, respectively. x_o is the thickness of dielectric layer, E_s is the surface electric field, and V_{fb} is the flat-band voltage depending on the metal-semiconductor workfunction difference.

The analysis of OFET devices is entirely different from MOSFETs. For a p-channel MOSFET working in enhancement mode, a negative bias is applied on the gate to create an inversion layer on the semiconductor-dielectric interface. The inversion layer on the interface will provide a conduction channel for the transports of minority carriers (i.e., holes in p-channel/pnp MOSFET.) between drain and source. In the enhancement-mode operation of a p-channel OFET, however, a negative gate bias V_{gs} will produce an accumulation layer on the semiconductor-dielectric interface, and the majority carriers in p-channel OFET, i.e., holes are transported within this accumulation layer. Fig. 4 demonstrates the relationships
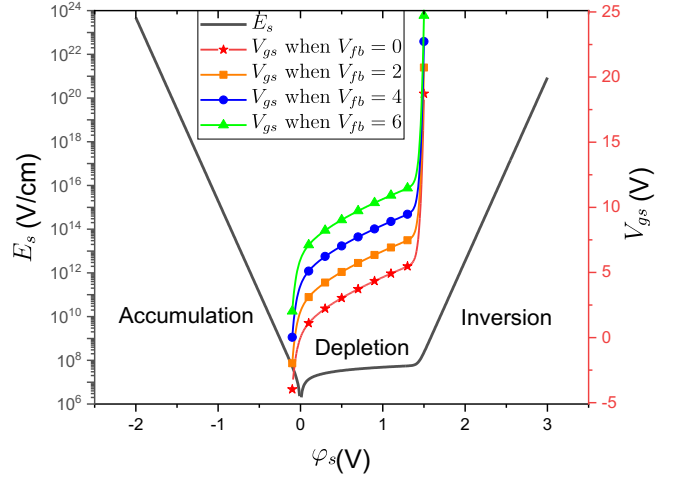

Fig. 4. Variation of surface electric field as a function of surface potential (left), gate voltage versus surface potential for different values of flat-band voltage, only cases with positive flat-band voltages are presented (right).

developed in (12) and (14). As we can see, the formation of an accumulation layer in a p-channel OFET requires a negative surface potential, and as a result, the gate voltage is also reversely biased when $V_{fb} = 0$. An additional observation is that the positively increased flat-band voltage may give rise to depletion-mode operation of OFET, in which a positive gate voltage needs to be applied to deplete the accumulation layer and turn the device off. For a nonideal OFET model, the relationship between V_{gs} and φ_s may slightly deviate from (14). For example, the V_{gs}-φ_s curves may shift left in Fig. 4 and the accumulation-depletion transition point will be negative ($\varphi_s < 0$) instead of zero. This nonideality results from the nonuniform distributions of surface potential (φ_s varies along x direction), the nonzero backside potentials and other systematic modeling errors. We will compensate this nonideality in the simulation by uniformly shifting φ_s left and applying gradual channel approximation to estimate the variation of φ_s along x direction.

B. Carrier Mobility Model

The effective carrier mobility in the active layer of an OFET is described by either the hopping energy model or the band-like carrier transport models [4], [41]. The hopping mechanism for charge carrier transport in disordered OSC was developed few decades ago [42], and recent research revealed that the hopping mechanism gives rise to a similar carrier mobility as the truly diffusive band-like transport models [43], [44]. In this work, the band-like transport models are adopted to model the effective carrier mobility in the organic DNTT. The carrier mobility within a semiconductor is inversely affected by multiple types of scattering events. For instance, the lattice scattering involves motion-impeding collisions between mobile carriers and thermally agitated lattice atoms, and the ionized impurity scattering results from the Coulombic interactions or direct collisions between mobile carriers and donor/acceptor-type trap sites. In the mobility modeling for semiconductors, different mobility models are usually required to be

concatenated in Matthiessen rule to account for distinct scattering effects in the channel. Specifically, for OSCs the ionized impurity scattering plays a dominant role in determining the overall effective mobility due to the existence of an enormous amount of ionized donor/acceptor-type trap sites in the carrier transport channel. A well-known mobility model for OSCs is the Poole-Frenkel (PF) model [45]. The PF model considers a field-induced exponential enhancement in the mobility and its expression is given in (15),

$$\mu_{PF} = \mu_0 \exp\left(-\frac{\Delta}{kT}\right) \exp\left[\left(\frac{\beta}{kT} - \gamma_{pf}\right)\sqrt{E_x}\right] \qquad (15)$$

where μ_0 is the zero-field nonactivated mobility related to OSC properties, Δ is the zero-field activation energy, β and γ_{pf} are fitting parameters, and E_x is the electric field parallel to the channel direction. The Coulombic interactions among trap sites and mobile carriers are characterized by Coulombic scattering model [46], which is given in (16) and (17),

$$\mu_{C,p} = \frac{N2P \cdot \left(\frac{T}{300}\right)^{1.5}}{N_{TD} \ln\left(1 + \gamma_{BHp}\right) - \frac{\gamma_{BHp}}{1 + \gamma_{BHp}}} \qquad (16)$$

and

$$\gamma_{BHp} = \frac{N1P}{N_h} \cdot \left(\frac{T}{300}\right)^{ALPHAp} \qquad (17)$$

where $N1P$, $N2P$ and $ALPHAp$ are fitting parameters in Coulombic scattering model, T is channel temperature in Kelvin, N_{TD} is the band-edge intercept density of TD traps, and N_h is the effective density of HOMO states. Besides these two models, an additional field-dependent mobility model to make sure the saturation of carrier drift velocity under high field should be considered, i.e., Caughey-Thomas (CT) model [47], and it is given in (18),

$$\mu_{CT} = \frac{\mu_0}{\left(1 + \left(\frac{\mu_0 E_{||}}{v_{Sat}}\right)^{BETACT}\right)^{\frac{1}{BETACT}}} \qquad (18)$$

where v_{Sat} is the saturated drift velocity in the parallel-to-channel direction for mobile carriers, $E_{||}$ is the parallel component of the electric field and $BETACT$ is the fitting parameter in CT model. According to Matthiessen rule, the overall effective mobility μ_{eff} in OFET is determined by (19).

$$\frac{1}{\mu_{eff}} = \frac{1}{\mu_{PF}} + \frac{1}{\mu_{C,p}} + \frac{1}{\mu_{CT}} \qquad (19)$$

The effective mobility of DNTT with different TD trap densities is calculated and the simulation results are shown in Fig. 5. It can be observed that the effective mobility of holes in DNTT is enhanced within the low field region ($E_{eff} < 4 \times 10^4$ V/cm). In high field region, the drift velocity of holes is limited
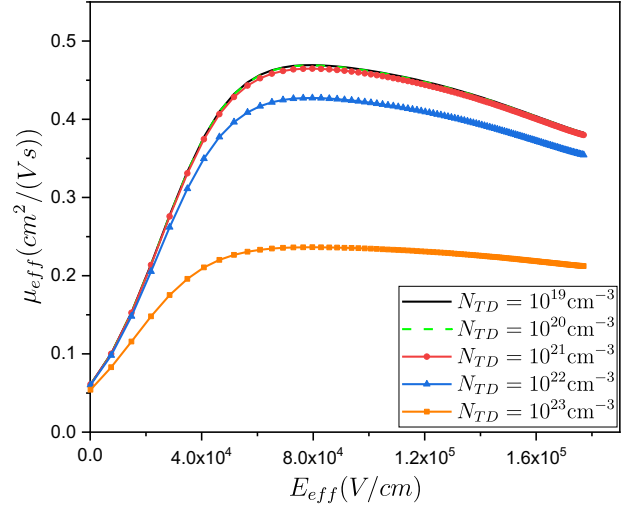

Fig. 5. Resultant effective mobility within DNTT versus effective electric field under different density of trap states.

and finally saturated as the motion impeding collisions among high-field accelerated holes and semiconductor surface, ionized trap sites or agitated lattice atoms become severe. While the drift velocity of holes is saturated in high field region, the effective mobility will demonstrate a tendency of degradation as electric field increases. In addition, Fig. 5 also presents the comparisons of resultant effective mobility of holes under the impacts of different TD trap densities. As indicated in Fig. 5, the adverse effects on the effective mobility of holes become evident as the density of TD trap states N_{TD} exceeds the effective density of HOMO states, which is $N_h = 2 \times 10^{21} \text{cm}^{-3}$ in our case. This decrease in mobility for increasing N_{TD} is reasonable since the increased density of trap states raises the probability for ionized impact scattering taking place in the DNTT.

C. Current-Voltage Model

Consider the OFET device shown in Fig. 3 with channel length L and channel width W. The thickness of the accumulation layer at location x is denoted by $y_a(x)$. Since in reality $y_a(x) \ll L$, we can neglect the changes of charge concentrations in the y direction and thus the electronic charge per cm^2 is given by $Q_p(x) = q \int_0^{y_a(x)}(p + g_{TD}^+)\mathrm{d}y \approx qy_a \cdot (p + g_{TD}^+)$. The positive charges in Q_p include mobile holes and ionized TD trap sites, and its relationship with applied gate bias and dielectric capacitance is given in (20),

$$Q_p(x) = C_{ox}\left(V_{gs} - V_{th} - V(x)\right) \qquad (20)$$

where C_{ox} is dielectric capacitance per unit area of gate, V_{gs} is the applied gate bias, V_{th} is the threshold voltage and $V(x)$ is the channel potential with respect to source along x direction. Substituting expressions for p and g_{TD}^+ from (2) and (9) into (20), we obtain the charge-voltage equation in (21).

$$p + p^{T/T_1}\left(\frac{N_{TD0}}{N_h^{T/T_1}}\right) = \frac{C_{ox}}{qy_a}\left(V_{gs} - V_{th} - V(x)\right) \qquad (21)$$

Since the density of ionized trap states is much larger than mobile hole (carrier) concentrations in OFET, the first term on the left of (21) can be neglected. Upon calculations, the carrier concentration in the channel is simplified as (22).

$$p = N_h\left[\frac{C_{ox}\left(V_{gs} - V_{th} - V(x)\right)}{qy_a N_{TD0}}\right]^{T_1/T} \qquad (22)$$

For a medium/long channel device, the carrier diffusion is negligible. In this response, we only consider the drift motion of carriers as the major source of current flow in the channel. If we further assume that the changes of electric field in x direction is trivial with respect to changes in y direction (i.e., gradual channel approximation), the channel current can be determined by (23).

$$I(x) = -\mu_{eff}Wq \cdot \left(\int_0^{y_a(x)} p(x,y)\mathrm{d}y\right) \cdot \frac{\mathrm{d}V(x)}{\mathrm{d}x} \qquad (23)$$

By substituting (22) into (23) and integrating both sides of (23), we get the channel current in (24),

$$I_D = \frac{(qy_a)^{1-\gamma}\mu_{eff}WN_hC_{ox}^\gamma}{(\gamma+1)LN_{TD0}^\gamma}\Big[\left(V_{ds} + V_{th} - V_{gs}\right)^{\gamma+1} \\ - \left(V_{th} - V_{gs}\right)^{\gamma+1}\Big] \qquad (24)$$

where $\gamma = T_1/T$ is the parameter to quantify the relative magnitude of trap state densities in the channel, and V_{ds} is the drain-to-source voltage drop. Furthermore, if we apply Taylor expansion to (24) about $V_{ds} = 0$ and preserve the first order terms in the expansion, it is found that (24) can be simplified to a more explanatory form shown in (25).

$$I_D = -\frac{(qy_a)^{1-\gamma}\mu_{eff}WN_hC_{ox}^\gamma}{LN_{TD0}^\gamma}\Big[\left(V_{gs} - V_{th}\right)V_{ds} \\ - \frac{\gamma}{2}V_{ds}^2\Big] \qquad (25)$$

Letting $\gamma = 1$, it can be easily proved that N_h and N_{TD0} are approximately the same in magnitude. Thus, the generalized current-voltage model in (24) and (25) for OFETs degenerates to the model for inorganic MOSFETs, as presented in (26).

$$I_D = -\frac{\mu_{eff}WC_{ox}}{L}\Big[\left(V_{gs} - V_{th}\right)V_{ds} - \frac{1}{2}V_{ds}^2\Big] \qquad (26)$$

When the magnitude of V_{ds} exceeds $\left(V_{gs} - V_{th}\right)$, the pinch-off will take place in the accumulation layer and the drain current will become saturated. The generalized current-voltage model in the saturation region is then given in (27).

TABLE I
MODEL PARAMETERS USED IN OFET EQUATIONS

Symbol	Quantity	Values Specified in Simulation
K_S	dielectric constant for semiconductor	3.0
K_O	dielectric constant for insulating materials	3.9
x_0	thickness of dielectric layer	64 nm $= 6.4 \times 10^{-7}$ cm
N_h	effective density of HOMO states	2×10^{21} cm^{-3}
L	channel length	100 μm
W	channel width	1000 μm
C_{OX}	dielectric capacitance per unit area	5.3955×10^{-8} F/cm^2
γ	relative trap states numbers	Variable $\sim 1, 1.1, 1.2, 1.3$
Δ	activation energy in Poole-Frenkel model	0.2 eV
β	fitting parameter in PF model	3.79×10^{-2} eV $\cdot \sqrt{cm/V}$
γ_{pf}	fitting parameter in PF model	1×10^{-5}
μ_0	free hole mobility	0.5 cm^2/(V $\cdot$ s)
$N1P$	fitting parameter in Coulombic scattering model	8.1×10^{11}
$N2P$	fitting parameter in CSM	4×10^{13}
$ALPHAp$	fitting parameter in CSM	3.4
N_{TD}	band-edge intercept of TD traps	$1 \times 10^{18} \sim 10^{23}$ cm^{-3}
γ_{BHp}	dependent parameter	4.05×10^{-10} cm^3
$BETACT$	fitting parameter in CT model	1
v_{Sat}	saturated velocity in CT model	640 cm/s
y_a	nominal thickness of the accumulation layer	5 nm $= 5 \times 10^{-7}$ cm
N_{TD0}	band-edge intercept of ionized TD traps	3.6×10^{20} cm^{-3}
d_s	thickness of substrate	154 nm $= 1.54 \times 10^{-5}$ cm
d_f	thickness of the active layer	30 nm
χ	the relative Young's modulus of active layer to substrate	15.36 GPa/2.8 GPa
η	the relative thickness of active layer to substrate	0.195
$\Pi(\theta,\varphi)$	Piezoresistive coefficient	7.57×10^{-9} Pa^{-1}
Ξ_d	dilation deformation potentials at HOMO edges	210.5 eV
Ξ_u	uniaxial deformation potentials at HOMO edges	330 eV
I_{D0}	leakage current	-4.139×10^{-3} μA（Pre-bent）-5.24×10^{-3} μA (Post-bent)
n	slope parameter	11.2/7.373 (Pre-/Post-bent)
α	fitting parameter	3.374/0.5551 (Pre-/Post-bent)

$$I_{DSat} = -\frac{(qy_a)^{1-\gamma}\mu_{eff}WN_hC_{ox}^\gamma}{(\gamma+1)LN_{TD0}^\gamma}\left(V_{th} - V_{gs}\right)^{\gamma+1} \qquad (27)$$

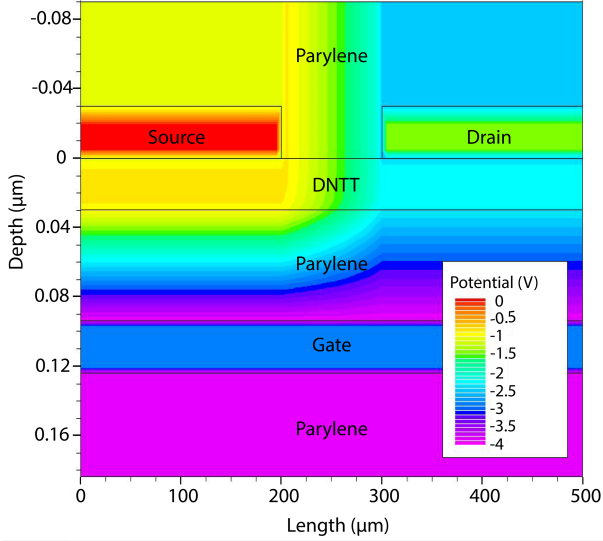In the derivation of the generalized Current-Voltage model

Fig. 6. Atlas 2D device simulated potential contour profile to explain the model working under applied bias $V_{ds} = -1.5\,V$ and $V_{gs} = -3\,V$.
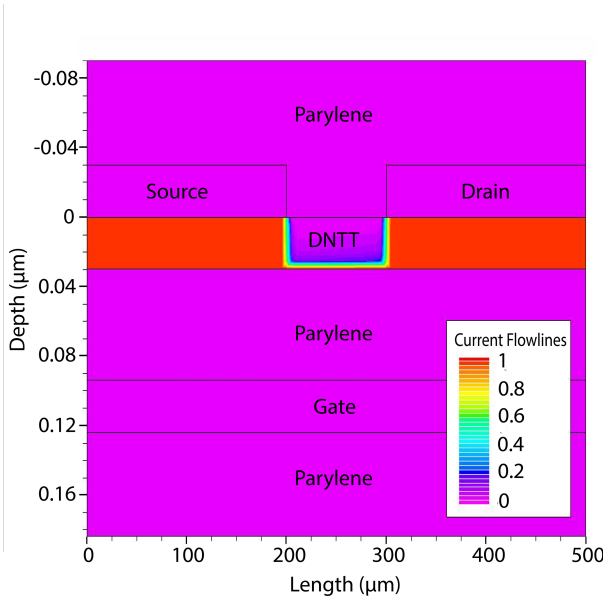

Fig. 7. Atlas 2D device simulated current flow contour profile shows the accumulation layer of the OFET model working under applied bias $V_{ds} = -1.5\,V$ and $V_{gs} = -3\,V$.

for OFETs, the thickness of the accumulation layer $y_a(x)$ may not be uniformly constant along x direction in real cases. Thus y_a in the model should be considered as the nominal thickness. It should be mentioned that the analytical model developed in this work cannot explain the OFET characteristics in the subthreshold regime. For Current-Voltage model in the subthreshold regime, we consider (28), a variant form of [48],

$$I_D = I_{D0} \cdot \left(\frac{V_{gs}}{V_T}\right)^\alpha \exp\left(\frac{V_{th} - V_{gs}}{nV_T}\right) \tag{28}$$

where I_{D0} is the leakage current, $V_T = kT/q$ is the thermal voltage, n is the slope parameter, and α is the fitting parameter.
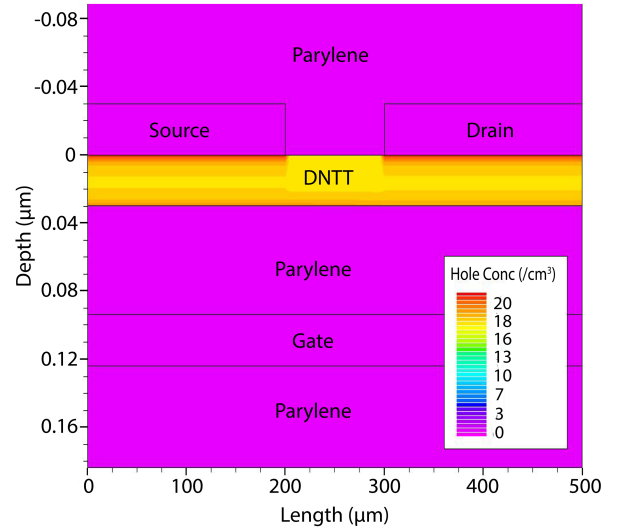

Fig. 8. Atlas 2D device simulated hole concentration contour profile under applied bias $V_{ds} = -1.5\,V$ and $V_{gs} = -3\,V$.

D. Electro-mechanical Coupling model

Strains inside the semiconductor can result from phonon-agitated lattice vibrations, lattice mismatches during film growth in epitaxial heterostructures, intrinsic strains in thin film depositions, and external loads [35]. The development of strain-induced electro-mechanical coupling relations is significantly more complicated in OFETs compared to MOSFETs since the bonding and antibonding mechanisms for organic materials bring more unprecedented modeling errors than inorganic materials (e.g., Si, Ge, GaAs, etc.) with periodical crystal structures. In this regard, we adopt method of superpositions and propose a semiempirical model to characterize the bending effects on electrical performance of OFETs. Consider the OFET model shown in Fig. 3, the mechanical strain developed on the top of the active layer is evaluated by (29) [49], [50],

$$\varepsilon = \left(\frac{d_s + d_f}{2R}\right) \frac{(1 + 2\chi\eta + \chi\eta^2)}{(1 + \eta)(1 + \chi\eta)} \tag{29}$$

where d_s and d_f are the thickness of substrate and active layer, respectively. χ is equal to Y_f/Y_s, the ratio of active layer's Young's moduli to substrate's Young's moduli. η is d_f/d_s and R is the bending radius (curvature). In the experiment [51], the substrate and dielectric layers are both Parylene, the gate (gold) electrode is negligible in thickness so we can treat the total thickness of the dielectric layer and the substrate layer as d_s in the calculation of bending strains. Implied by Drude's mobility model, strain impacts on mobility by interfering the scattering process. The interfering mechanism in MOSFETs can be mathematically formulated with the help of quantum mechanics [34], [35]. In this work, we brief those convoluted quantum descriptions, and it is found that a semiempirical expression in (30) can be utilized to correlate surface strain ε and mobility shift $\Delta\mu_{eff}$,
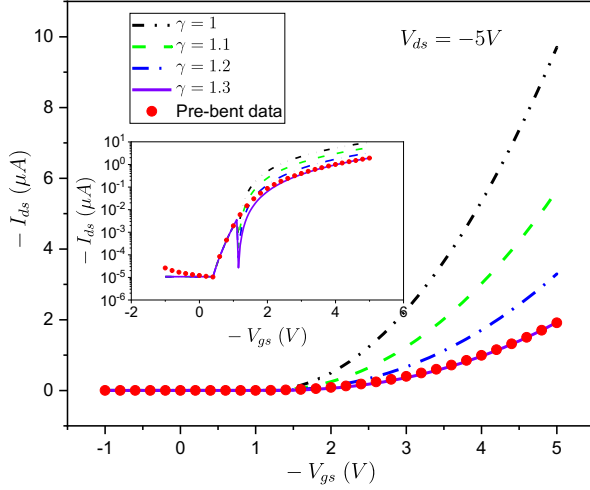
Fig. 9. Drain current versus gate-source voltage characteristics under different γ values, the theoretical curve with $\gamma = 1.3$ is in good consistence with pre-bent experimental data. V_{ds} is fixed to -5 V.
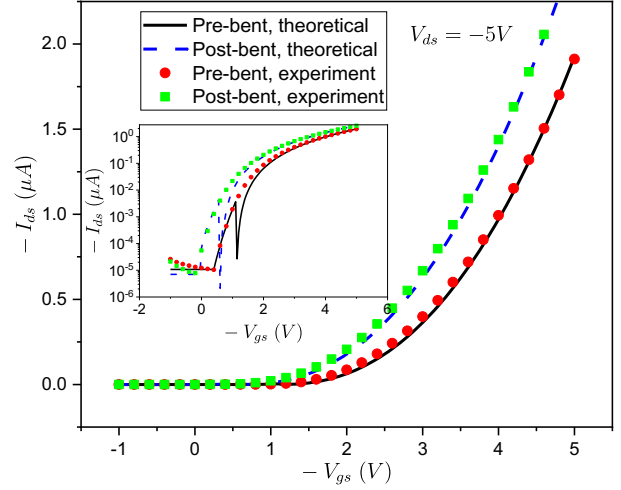

Fig. 11. Comparison of measured (symbols) and generalized theoretically modeled ($\gamma = 1.3$) drain current as a function of source-gate voltage for fixed $V_{ds} = -5$ V, both pre-bent and post-bent cases are illustrated.
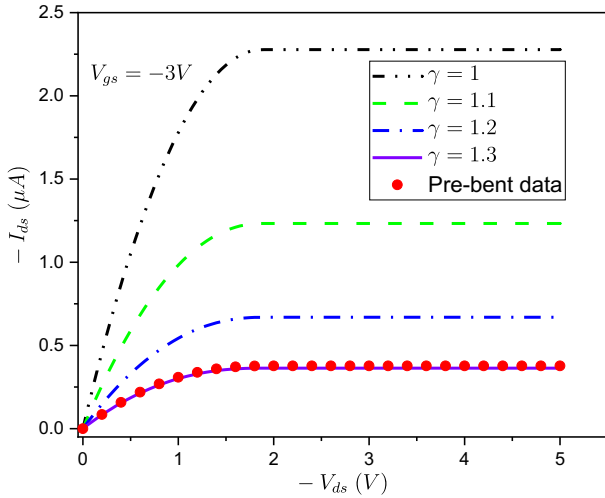
where ΔE_{HOMO} is the shift of HOMO band due to strain, ΔE_g is the change of band gap, $N_l(\varepsilon)$ is the effective LUMO density of states under strain ε, and m ($\sim 1.2 - 1.4$) is the body-effect coefficient. For a p-type OFET, the contribution from LUMO band is too small so that the last term in (31) can be neglected. The deformation potential theory gives the shifts on HOMO band and band gap as (32) [53],

$$\Delta \mathrm{E}_g \approx \Delta E_{HOMO} = \left(\Xi_d + \frac{1}{3}\Xi_u \right) \cdot tr(\varepsilon) \tag{32}$$

where Ξ_d, Ξ_u are dilation and uniaxial deformation potentials at the HOMO band edges. $tr(\varepsilon)$ is the trace of strain tensor. By superposing $\Delta\mu_{eff}$ and ΔV_{th} to (24) and (27), the bending induced variations on the transconductance of a p-type OFET can be quantitatively characterized. Therefore, the pre- and post-bent characteristics can be simulated with the help of a system of equations formed by (19), (24), (27), (28), (30) and (31).

Fig. 10. Drain current versus drain-source voltage characteristics under different γ values, the theoretical curve with $\gamma = 1.3$ is in good consistence with pre-bent experimental data. V_{gs} is fixed to -3 V.

III. EXPERIMENTAL VERIFICATION AND DISCUSSIONS

The basic components of a BGTC OFET are sketched in Fig. 3. The bending test is achieved by laminating the encapsulated OFET onto a pre-stretched elastomer, which is then relaxed. The film forms wrinkles due to stress/strain at the interface of soft-but-thick elastomer and hard-but-thin OFET stack [13], with the conformal nature of the lamination correlated with the film thickness. The minimum bending radius (radius of curvature) is estimated at ~ 2 μm from SEM images. The fabrication and bending details are specified in [51].

To validate the theoretical model, we implement the simulation in Silvaco Atlas and extract fitting parameters by inspecting the measured transconductance curves. Silvaco Atlas can solve Poisson-Nernst-Planck (PNP) system of PDEs at each node in a two-dimensional meshed domain, with its boundary conditions automatically implemented in the software core [41]. The modeling/fitting parameters, material properties of organic

$$\frac{\Delta I_D}{I_D} \cong \frac{\Delta\mu_{eff}}{\mu_{eff}} = \Pi(\theta, \varphi) \cdot C\varepsilon \tag{30}$$

where $\Pi(\theta, \varphi)$ is the piezoresistive coefficient, θ and φ are parametric angles dependent on the crystalline structure and manufacturing layouts of semiconductors. C is the normalized stiffness constant and ε is the surface strain.

Strain also affects threshold voltage in another way. The channel strain will alter the band structure, including the ending conduction/valence band splitting, energy gap narrowing and band warping, etc [35]. It was proven that the threshold voltage shift due to strain is given by (31) [52],

$$\Delta V_{th} = \frac{1}{q}\left\{ \Delta E_{HOMO} + (m-1)\left[\Delta E_g + kT \cdot \log\frac{N_l(0)}{N_l(\varepsilon)} \right] \right\} \tag{31}$$

Fig. 12. Comparison of measured (symbols) and generalized theoretically modeled ($\gamma = 1.3$) drain current as a function of drain-source voltage for fixed $V_{gs} = 0, -1, -2, -3, -4, -5$ V, the pre-bent case is illustrated.
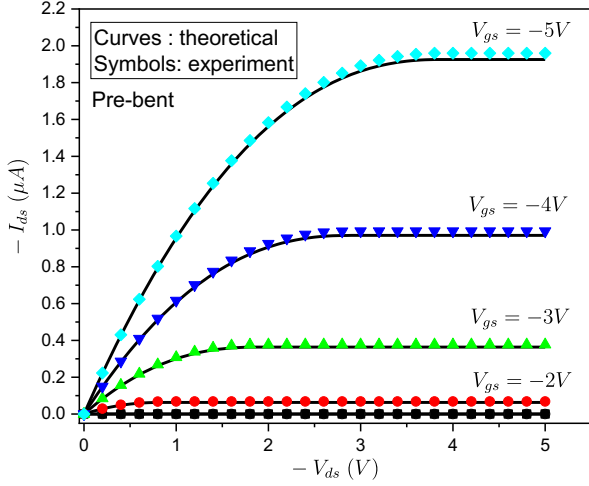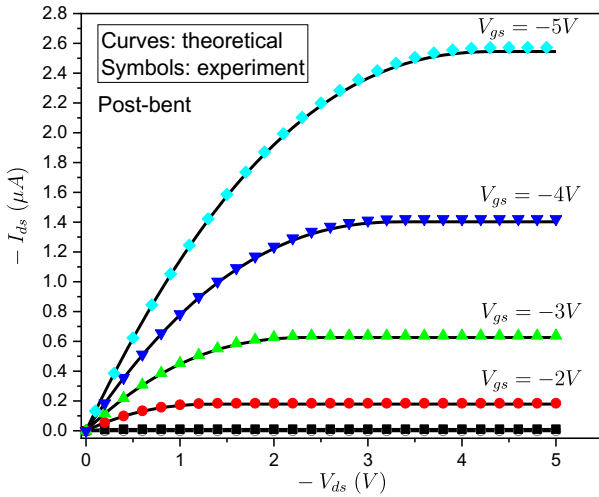

Fig. 13. Comparison of measured (symbols) and generalized theoretically modeled ($\gamma = 1.3$) drain current as a function of drain-source voltage for fixed $V_{gs} = 0, -1, -2, -3, -4, -5$ V, the post-bent case is illustrated.

semiconductors and dielectric materials are summarized and listed in Table 1. The simulated potential contour plot and the current flowlines in the OFET operated under applied bias $V_{ds} = -1.5$ V and $V_{gs} = -3$ V, are shown in Fig. 6 and Fig. 7, respectively. It can be observed in Fig. 6 that the variation of potentials in the channel along x direction is more evident than its changes along y direction. This is due to the gradual channel approximation adopted in the current-voltage model. Since the channel length is much larger than the channel thickness, a comprehensive potential drop along x direction may still give rise to a trivial parallel electric field in comparison to its perpendicular component. As depicted in Fig. 3, the OFET should maintain an accumulation layer on the surface of the dielectric-semiconductor interface to provide a surface channel

for current flows. Fig. 7 demonstrates the simulated contour of the accumulation layer and suggests that the thickness of the accumulation layer should be around 5 nm in our case, which agrees with [54]–[56]. Fig. 8 portrays steady state hole concentrations in the OFET, which implies that the recombination of the majority charge carriers is way more active than their generation in OSCs.

Fig. 9 shows a transconductance curve, that plots the drain current versus gate-source voltage, under different γ values, and Fig. 10 displays the output curve, that plots the drain current versus drain-source voltage, under different γ values. With γ increasing from 1 to 1.3, the density of trap states emulates and exceeds the density of LUMO states. The immense number of ionized trap sites will impede the hole transports and reduce the drain current flows in the channel. As a result, the drain current in $\gamma = 1.3$ is reduced to about 1/9 of the drain current in $\gamma = 1$. Moreover, it can be observed that the theoretical curve for $\gamma = 1.3$ also demonstrates a better fit to the pre-bent experimental data except for the vicinity around the threshold voltage, which implies that the generalized theoretical model when $\gamma = 1.3$ can accurately simulate the quantity of traps in our real OFET in the linear and saturation regimes. The trap concentration in the generalized theoretical model can be adjusted by γ and N_{TD}, independently. The levels of N_{TD} can influence the magnitude of carrier mobilities, as we discussed previously in the establishment of the mobility models. The values of γ, in another way, modify the OFET transconductance characteristics by directly maneuvering the generalized current-voltage model.

Fig. 11 compares the measured (red circles and green squares) and the theoretically modeled (black solid and blue dashed lines) I_{ds} versus V_{gs} characteristics, both for the cases of pre- and post-bent OFETs, with V_{ds} fixed to -5 V. In the theoretical model, we consider the strain-induced shifts in the threshold voltage and the carrier mobility by superposing the results of (30) and (31) to (24) and (27). It can be seen that the theoretical model ($\gamma = 1.3$) validated in the pre-bent case is also valid for the post-bent case if we set the electro-mechanical coupling model with parameters listed in Table 1. The pre- and post-bent theoretical models are both produced with the ionized TD trap density $N_{TD0} = 3.6 \times 10^{20}$ cm^{-3}. The TD trap density N_{TD} is determined by N_{TD0} and γ according to (10), and the resultant effective mobility within DNTT is then adjusted by N_{TD}. However, it should be noted that the theoretical model is much better fitting the experimental measurements at the high V_{gs} region (i.e., linear and saturation regimes). As demonstrated by the inset transconductance curves in Fig. 11, our model fails within a small transitional region between subthreshold regime and linear/saturation regimes. This is because at the high V_{gs} region, the Fermi level is bent towards to the band edge of LUMO, leading to a closer distance between TD trap sites and LUMO edges. In this sense, the capturing and decapturing of holes in TD traps will prevail among all four types of trapping activities (i.e., TD, TA, GD, GA.). At the low V_{gs} region, the Fermi level is positioned close to deep level trap states, and thus GA and GD traps will play more important roles than TD traps in the trapping and detrapping of carriers. Since we also utilize (28) to remedy the OFET behaviors in the subthreshold regime,

our model only loses its control within a small transitional V_{gs} region.

Fig. 12 compares the measured (red circles and green squares) and the theoretically modeled (black solid and blue dashed lines) I_{ds} versus V_{ds} characteristics, for the case of pre-bent OFETs, with V_{gs} fixed to $0, -1, -2, -3, -4$ and -5 V, respectively. Similarly, the post-bent I_{ds} versus V_{ds} characteristics under different fixed V_{gs} is sketched in Fig. 13. It is shown in both figures that the generalized theoretical models ($\gamma = 1.3$) are in good agreement with the measured experimental data. Further analysis reveals that the non-effective mobility μ_{eff} is enhanced from $0.5\ \text{cm}^2/(\text{V} \cdot \text{s})$ to $0.57\ \text{cm}^2/(\text{V} \cdot \text{s})$, with average effective mobility increased from $0.43\ \text{cm}^2/(\text{V} \cdot \text{s})$ to $0.49\ \text{cm}^2/(\text{V} \cdot \text{s})$, and the threshold voltage V_{th} is shifted from -1.12 V to -0.62 V, if we compare the pre- and the post-bent transconductance curves. Another important observation is that I_{ds} is no longer zero for $V_{gs} = -1$ V, due to the magnitude of the threshold voltage shrinking to less than V_{gs} when bending takes effects.

IV. CONCLUSION

An analytical model to characterize the electrical properties of a bendable OFET is presented in this paper. The model is developed by considering the trap states in the OSCs and incorporating the stress-induced shifts on the effective mobility and the threshold voltage into the generalized current-voltage model. With the p-type OFET operating in enhancement mode, an accumulation layer is formed within the semiconductor at the interface with the dielectric layer, to transport the majority carriers (i.e., holes) between source and drain electrodes. The concatenation of field-dependent Poole-Frenkel model, Coulombic scattering model, and Caughey-Thomas model in the Matthiessen's style, is an effective way to account for the effective mobility with enhancement behavior in the low-field region and degradation behavior in the high-field region. The levels of trap states in the generalized current-voltage model can be adjusted by varying parameter γ in the equations. It is verified that the generalized physical model when $\gamma = 1.3$ can accurately explain the experimental measurements for both the pre-bent and post-bent DNTT-based OFETs in the linear and saturation regimes. The generalized OFET model is physically based, and the model parameters can be easily extracted or quickly fitted from limited experimental data. Likewise, the bendable OFETs with different layouts, or made from different OSCs, can also be precisely characterized by this generalized model. Another contribution of this work is that our model can predict the stress-induced behaviors of the OFET devices with different bending radii.

ACKNOWLEDGMENT

REFERENCES

[1] C. D. Dimitrakopoulos and D. J. Mascaro, "Organic thin-film transistors: A review of recent advances," *IBM J. Res. Dev.*, vol. 45, no. 1, pp. 11–27, 2001, doi: 10.1147/rd.451.0011.

[2] C. D. Dimitrakopoulos and P. R. L. Malenfant, "Organic Thin Film Transistors for Large Area Electronics," *Adv. Mater.*, vol. 14, no. 2, pp. 99–117, Jan. 2002, doi: 10.1002/1521-4095(20020116)14:2<99::AID-ADMA99>3.0.CO;2-9.

[3] Y. Y. Lin, D. J. Gundlach, S. F. Nelson, and T. N. Jackson, "Pentacene-based organic thin-film transistors," *IEEE Trans. Electron Devices*, vol. 44, no. 8, pp. 1325–1331, 1997, doi: 10.1109/16.605476.

[4] G. Horowitz, "Organic Field-Effect Transistors," *Adv. Mater.*, vol. 10, no. 5, pp. 365–377, Mar. 1998, doi: 10.1002/(SICI)1521-4095(199803)10:5<365::AID-ADMA365>3.0.CO;2-U.

[5] G. Horowitz, "Organic thin film transistors: From theory to real devices," *J. Mater. Res.*, vol. 19, no. 7, pp. 1946–1962, Jul. 2004, doi: 10.1557/JMR.2004.0266.

[6] F. Ebisawa, T. Kurokawa, and S. Nara, "Electrical properties of polyacetylene/polysiloxane interface," *J. Appl. Phys.*, vol. 54, no. 6, pp. 3255–3259, Jun. 1983, doi: 10.1063/1.332488.

[7] F. Garnier, G. Horowitz, X. Peng, and D. Fichou, "An all-organic 'soft' thin film transistor with very high carrier mobility," *Adv. Mater.*, vol. 2, no. 12, pp. 592–594, Dec. 1990, doi: 10.1002/adma.19900021207.

[8] J. A. Rogers *et al.*, "Paper-like electronic displays: Large-area rubber-stamped plastic sheets of electronics and microencapsulated electrophoretic inks," *Proc. Natl. Acad. Sci. U. S. A.*, vol. 98, no. 9, pp. 4835–4840, Apr. 2001, doi: 10.1073/pnas.091588098.

[9] C. Zhu, H. C. Wu, G. Nyikayaramba, Z. Bao, and B. Murmann, "Intrinsically Stretchable Temperature Sensor Based on Organic Thin-Film Transistors," *IEEE Electron Device Lett.*, vol. 40, no. 10, pp. 1630–1633, Oct. 2019, doi: 10.1109/LED.2019.2933838.

[10] S. E. Root, S. Savagatrup, A. D. Printz, D. Rodriquez, and D. J. Lipomi, "Mechanical Properties of Organic Semiconductors for Stretchable, Highly Flexible, and Mechanically Robust Electronics," *Chemical Reviews*, vol. 117, no. 9. American Chemical Society, pp. 6467–6499, 10-May-2017, doi: 10.1021/acs.chemrev.7b00003.

[11] M. H. Lee, B. F. Hsieh, and S. T. Chang, "Electrical properties correlated with redistributed deep states in a-Si:H thin-film transistors on flexible substrates undergoing mechanical bending," in *Thin Solid Films*, 2013, vol. 528, pp. 82–85, doi: 10.1016/j.tsf.2012.10.097.

[12] J. Zhang *et al.*, "Flexible Oxide-Based Thin-Film Transistors on Plastic Substrates for Logic Applications," *J. Mater. Sci. Technol.*, vol. 31, no. 2, pp. 171–174, Feb. 2015, doi: 10.1016/j.jmst.2014.07.009.

[13] R. A. Nawrocki, "Super- and Ultrathin Organic Field-Effect Transistors: from Flexibility to Super- and Ultraflexibility," *Adv. Funct. Mater.*, vol. 29, no. 51, p. 1906908, Dec. 2019, doi: 10.1002/adfm.201906908.

[14] R. F. Pierret, *Semiconductor Device Fundamentals*. Addison-Wesley, 1996.

[15] M. A. Alam, A. Dodabalapur, and M. R. Pinto, "A two-dimensional simulation of organic transistors," *IEEE Trans. Electron Devices*, vol. 44, no. 8, pp. 1332–1337, 1997, doi: 10.1109/16.605477.

[16] P. V. Necliudov, M. S. Shur, D. J. Gundlach, and T. N. Jackson, "Modeling of organic thin film transistors of different designs," *J. Appl. Phys.*, vol. 88, no. 11, pp. 6594–6597, Dec. 2000, doi: 10.1063/1.1323534.

[17] M. Fadlallah, G. Billiot, W. Eccleston, and D. Barclay, "DC/AC unified OTFT compact modeling and circuit design for RFID applications," *Solid. State. Electron.*, vol. 51, no. 7, pp. 1047–1051, Jul. 2007, doi: 10.1016/j.sse.2007.05.018.

[18] R. M. Meixner *et al.*, "A physical-based PSPICE compact model for poly(3-hexylthiophene) organic field-effect transistors," *IEEE Trans. Electron Devices*, vol. 55, no. 7, pp. 1776–1781, Jul. 2008, doi: 10.1109/TED.2008.925339.

[19] S. Locci, M. Morana, E. Orgiu, A. Bonfiglio, and P. Lugli, "Modeling of short-channel effects in organic thin-film transistors," *IEEE Trans. Electron Devices*, vol. 55, no. 10, pp. 2561–2567, 2008, doi: 10.1109/TED.2008.2003022.

[20] M. C. Hamilton, S. Martin, and J. Kanicki, "Field-effect mobility of organic polymer thin-film transistors," *Chem. Mater.*, vol. 16, no. 23, pp. 4699–4704, Nov. 2004, doi: 10.1021/cm049613r.

[21] G. Horowitz, "Interfaces in Organic Field-Effect Transistors," Springer, Berlin, Heidelberg, 2009, pp. 113–153.

[22] E. G. Bittle, J. I. Basham, T. N. Jackson, O. D. Jurchescu, and D. J.

Gundlach, "Mobility overestimation due to gated contacts in organic field-effect transistors," *Nat. Commun.*, vol. 7, no. 1, pp. 1–7, Mar. 2016, doi: 10.1038/ncomms10908.

[23] D. Gupta, N. Jeon, and S. Yoo, "Modeling the electrical characteristics of TIPS-pentacene thin-film transistors: Effect of contact barrier, field-dependent mobility, and traps," *Org. Electron.*, vol. 9, no. 6, pp. 1026–1031, Dec. 2008, doi: 10.1016/j.orgel.2008.08.005.

[24] W. Wondmagegn and R. Pieper, "Simulation of top-contact pentacene thin film transistor," *J. Comput. Electron.*, vol. 8, no. 1, pp. 19–24, Apr. 2009, doi: 10.1007/s10825-009-0265-3.

[25] L. Li, H. Marien, J. Genoe, M. Steyaert, and P. Heremans, "Compact model for organic thin-film transistor," *IEEE Electron Device Lett.*, vol. 31, no. 3, pp. 210–212, Mar. 2010, doi: 10.1109/LED.2009.2039744.

[26] T. K. Maiti *et al.*, "A surface potential based organic thin-film transistor model for circuit simulation verified with DNTT high performance test devices," *IEEE Trans. Semicond. Manuf.*, vol. 27, no. 2, pp. 159–168, 2014, doi: 10.1109/TSM.2014.2304736.

[27] F. Ana and N. ud Din, "Design and performance investigation of short channel bottom-contact organic thin-film transistors," *J. Comput. Electron.*, vol. 17, no. 3, pp. 1315–1323, Sep. 2018, doi: 10.1007/s10825-018-1170-4.

[28] F. Ana and Najeeb-ud-Din, "An analytical modeling approach to the electrical behavior of the bottom-contact organic thin-film transistors in presence of the trap states," *J. Comput. Electron.*, vol. 18, no. 2, pp. 543–552, Jun. 2019, doi: 10.1007/s10825-019-01314-6.

[29] A. D. D. Dwivedi, S. K. Jain, R. D. Dwivedi, and S. Dadhich, "Numerical simulation and compact modeling of low voltage pentacene based OTFTs," *J. Sci. Adv. Mater. Devices*, vol. 4, no. 4, pp. 561–567, Dec. 2019, doi: 10.1016/j.jsamd.2019.10.006.

[30] M. Grünewald, P. Thomas, and D. Würtz, "A Simple Scheme for Evaluating Field Effect Data," *Phys. status solidi*, vol. 100, no. 2, pp. K139–K143, Aug. 1980, doi: 10.1002/pssb.2221000253.

[31] W. L. Kalb and B. Batlogg, "Calculating the trap density of states in organic field-effect transistors from experiment: A comparison of different methods," *Phys. Rev. B - Condens. Matter Mater. Phys.*, vol. 81, no. 3, p. 035327, Jan. 2010, doi: 10.1103/PhysRevB.81.035327.

[32] C. Tserbak, H. M. Polatoglou, and G. Theodorou, "Unified approach to the electronic structure of strained Si/Ge superlattices," *Phys. Rev. B*, vol. 47, no. 12, pp. 7104–7124, 1993, doi: 10.1103/PhysRevB.47.7104.

[33] M. V. Fischetti and S. E. Laux, "Band structure, deformation potentials, and carrier mobility in strained Si Ge, and SiGe alloys," *J. Appl. Phys.*, vol. 80, no. 4, pp. 2234–2252, Aug. 1996, doi: 10.1063/1.363052.

[34] Y. Sun, S. E. Thompson, and T. Nishida, "Physics of strain effects in semiconductors and metal-oxide-semiconductor field-effect transistors," *J. Appl. Phys.*, vol. 101, no. 10, p. 104503, May 2007, doi: 10.1063/1.2730561.

[35] Y. Sun, S. E. Thompson, and T. Nishida, *Strain effect in semiconductors: Theory and device applications*. Springer US, 2010.

[36] N. Wacker, H. Richter, M. U. Hassan, H. Rempp, and J. N. Burghartz, "Compact modeling of CMOS transistors under variable uniaxial stress," *Solid. State. Electron.*, vol. 57, no. 1, pp. 52–60, Mar. 2011, doi: 10.1016/j.sse.2010.12.003.

[37] Z. Wang, S. Chen, X. Duan, D. Sun, and X. Gong, "Strain induced quantum effect in semiconductors," *J. Phys. Soc. Japan*, vol. 81, no. 7, Jul. 2012, doi: 10.1143/JPSJ.81.074712.

[38] M. Gunda, P. Kumar, and M. Katiyar, "Review of Mechanical Characterization Techniques for Thin Films Used in Flexible Electronics," *Critical Reviews in Solid State and Materials Sciences*, vol. 42, no. 2. Taylor and Francis Inc., pp. 129–152, 04-Mar-2017, doi: 10.1080/10408436.2016.1186006.

[39] T. B. Singh, N. S. Sariciftci, and J. G. Grote, "Bio-Organic Optoelectronic Devices Using DNA," *Springer, Berlin, Heidelberg*, 2009, pp. 73–112.

[40] F. F. Vidor, T. Meyers, and U. Hilleringmann, "Inverter circuits using ZnO nanoparticle based thin-film transistors for flexible electronic applications," *Nanomaterials*, vol. 6, no. 9, Sep. 2016, doi: 10.3390/nano6090154.

[41] Silvaco International, "Atlas Users Manual," 2016. [Online]. Available: https://dynamic.silvaco.com/dynamicweb/jsp/downloads/Download ManualsAction.do?req=silen-manuals&nm=atlas. [Accessed: 15-May-2020].

[42] A. H. A. El Ela and H. H. Afifi, "Hopping transport in organic semiconductor system," *J. Phys. Chem. Solids*, vol. 40, no. 4, pp. 257–259, Jan. 1979, doi: 10.1016/0022-3697(79)90100-8.

[43] S. Wang, M. Ha, M. Manno, C. Daniel Frisbie, and C. Leighton, "Hopping transport and the Hall effect near the insulator-metal transition in electrochemically gated poly(3-hexylthiophene) transistors," *Nat. Commun.*, vol. 3, no. 1, pp. 1–7, Nov. 2012, doi: 10.1038/ncomms2213.

[44] S. Giannini, A. Carof, and J. Blumberger, "Crossover from Hopping to Band-Like Charge Transport in an Organic Semiconductor Model: Atomistic Nonadiabatic Molecular Dynamics Simulation," *J. Phys. Chem. Lett.*, vol. 9, no. 11, pp. 3116–3123, Jun. 2018, doi: 10.1021/acs.jpclett.8b01112.

[45] W. D. Gill, "Drift mobilities in amorphous charge-transfer complexes of trinitrofluorenone and poly-n-vinylcarbazole," *J. Appl. Phys.*, vol. 43, no. 12, pp. 5033–5040, Dec. 1972, doi: 10.1063/1.1661065.

[46] H. Shin, A. F. Tasch, C. M. Maziar, and S. K. Banerjee, "A New Approach to Verify and Derive a Transverse-Field-Dependent Mobility Model for Electrons in MOS Inversion Layers," *IEEE Trans. Electron Devices*, vol. 36, no. 6, pp. 1117–1124, 1989, doi: 10.1109/16.24356.

[47] D. M. Caughey and R. E. Thomas, "Carrier Mobilities in Silicon Empirically Related to Doping and Field," *Proc. IEEE*, vol. 55, no. 12, pp. 2192–2193, 1967, doi: 10.1109/PROC.1967.6123.

[48] P. R. van der Meer, A. van Staveren, and A. H. M. van Roermund, *Low-power deep sub-micron CMOS logic : sub-threshold current reduction*. Kluwer Academic, 2004.

[49] K. Fukuda *et al.*, "Strain sensitivity and durability in p-type and n-type organic thin-film transistors with printed silver electrodes," *Sci. Rep.*, vol. 3, no. 1, pp. 1–6, Jun. 2013, doi: 10.1038/srep02048.

[50] J. Oh *et al.*, "Bending Performance of Flexible Organic Thin-Film Transistors With/Without Encapsulation Layer," *IEEE Trans. Device Mater. Reliab.*, vol. 18, no. 1, pp. 1–4, Mar. 2018, doi: 10.1109/TDMR.2017.2780267.

[51] R. A. Nawrocki, N. Matsuhisa, T. Yokota, and T. Someya, "300-nm Imperceptible, Ultraflexible, and Biocompatible e-Skin Fit with Tactile Sensors and Organic Transistors," *Adv. Electron. Mater.*, vol. 2, no. 4, p. 1500452, Apr. 2016, doi: 10.1002/aelm.201500452.

[52] J. S. Lim, S. E. Thompson, and J. G. Fossum, "Comparison of threshold-voltage shifts for uniaxial and biaxial tensile-stressed n-MOSFETs," *IEEE Electron Device Lett.*, vol. 25, no. 11, pp. 731–733, Nov. 2004, doi: 10.1109/LED.2004.837581.

[53] Y. Yang, R. Nawrocki, R. Voyles, and H. H. Zhang, "Modeling of an Internal Stress and Strain Distribution of an Inverted Staggered Thin-Film Transistor Based on Two-Dimensional Mass-Spring-Damper Structure," *Comput. Model. Eng. & Sci.*, vol. NA, no. NA, 2020.

[54] D. Gupta, M. Katiyar, and D. Gupta, "An analysis of the difference in behavior of top and bottom contact organic thin film transistors using device simulation," *Org. Electron.*, vol. 10, no. 5, pp. 775–784, Aug. 2009, doi: 10.1016/j.orgel.2009.03.012.

[55] C. H. Shim, F. Maruoka, and R. Hattori, "Structural analysis on organic thin-film transistor with device simulation," *IEEE Trans. Electron Devices*, vol. 57, no. 1, pp. 195–200, Jan. 2010, doi: 10.1109/TED.2009.2035540.

[56] B. K. Kaushik, Brijesh Kumar, S. Prajapati, and P. Mittal, *Organic Thin-Film Transistor Applications : Materials to Circuits*, 1st ed., vol. 1. CRC Press, 2016.